Available online at www.sciencedirect.com
SCIENCE DIRECT®
Journal of Computational Physics 187 (2003) 441–456
JOURNAL OF COMPUTATIONAL PHYSICS
www.elsevier.com/locate/jcp

Laminar unsteady flows of Bingham fluids: a numerical strategy and some benchmark results

D. Vola *, L. Boscardin, J.C. Latché

Département de Recherche en Sécurité, Institut de Radioprotection et de Sûreté Nucléaire (IRSN), BP3-13115 St. Paul-lez-Durance Cedex, France

Received 20 November 2002; received in revised form 7 February 2003; accepted 17 February 2003

Abstract

We propose a numerical method to calculate unsteady flows of Bingham fluids without any regularization of the constitutive law. The strategy is based on the combination of the characteristic/Galerkin method to cope with convection and of the Fortin–Glowinsky decomposition/coordination method to deal with the non-differentiable and non-linear terms that derive from the constitutive law. For the spatial discretization, we use low order finite elements, with, in particular, linear discretization for the velocity and the pressure, stabilized by a Brezzi–Pitkäranta perturbation term. We illustrate this numerical strategy through two well-known problems, namely the hydrodynamic benchmark of the lid-driven cavity and the natural convection benchmark of the differentially heated cavity. For both, we assess our numerical scheme against previous publications, for Newtonian flow or in the creeping flow regime, and propose novel results in the case of Bingham fluid non-creeping flows.

AMS: 76D05; 76A05; 35R45; 65M25; 65M60

Keywords: Bingham fluids; Unsteady flows; Characteristic/Galerkin method; Decomposition/coordination method; Mixed finite elements; Brezzi–Pitkäranta stabilization; Lid-driven cavity; Thermally driven cavity; Benchmarking

1. Introduction

The linear Newtonian strain/stress relation appears to model the rheological behaviour of numerous industrial or geophysical flows poorly; this is the case for instance, of solidifying flows to be dealt with in nuclear safety studies, which is the context of the present work. Among the non-Newtonian fluids, the viscoplastic ones exhibit a yield stress and thus combine the behavior of solids in the so-called "rigid" regions and of non-Newtonian liquids in the "flow" regions. The internal dissipation potential defined by $\psi = \sigma{:}D$ is classically shown for isothermal flows of incompressible fluids to depend only on the second

* Corresponding author. Tel.: +33-4-4225-6350; fax: +33-4-4225-6143.
E-mail address: didier.vola@irsn.fr (D. Vola).

0021-9991/03/$ - see front matter
doi:10.1016/S0021-9991(03)00118-9

principal invariant $|D|$ of the shear strain rate tensor ($\sigma{:}D = \sum_{i,j} \sigma_{ij} D_{ij}$ and $|D|^2 = \|D\|^2_{\mathbb{R}^{2\times 2}} = \sum_{i,j} D_{ij} D_{ij}$). For the Bingham model, it is given by

$$\psi(D) = \mu |D|^2 + \tau_Y |D|, \tag{1}$$

The function ψ is not differentiable but is convex, lower-semicontinuous and positive. It is a pseudo-potential and the constitutive law can be expressed as the generalized equation

$$\tau = \sigma + pI \in \partial_D \psi. \tag{2}$$

Then by using the definition of sub-gradient $\partial_D \psi$, we can turn relations (1) and (2) to system (3) where the implicit splitting of the fluid domain into its "flow" and "rigid" parts explicitly appears as

$$\begin{cases} \text{if } |\tau| \geqslant \tau_Y & \tau = \left(\dfrac{\tau_Y}{|D|} + 2\mu \right) D, \\ \text{if } |\tau| \leqslant \tau_Y & D = 0. \end{cases} \tag{3}$$

This concludes out presentation of the governing set of equations. We will assume that the fluid is homogeneous and isotropic and that the fluid domain is an open and bounded subset of the physical space.

Nomenclature			
u	velocity field	D	shear strain rate tensor
σ	Cauchy stress tensor	μ	dynamic viscosity
p	pressure	ρ	density
τ	shear stress tensor	τ_Y	plasticity threshold
ψ	internal dissipation potential	g	gravity field

Fluid motion is governed by the Navier–Stokes set of equations, i.e., by the balance equation of momentum:

$$\rho \left(\frac{\partial u}{\partial t} + (u.\nabla) u \right) - \nabla \cdot \sigma = \rho g, \tag{4}$$

by continuity equation:

$$\nabla \cdot u = 0, \tag{5}$$

by Dirichlet homogeneous boundary conditions on the Lipschitz domain boundary $\partial\Omega$ and by the constitutive relations (1) and (2) or (3). For non-isothermal problems, this system must be complemented by an energy balance equation.

From relations (4), (1), (2) and (5), we can exhibit the three main difficulties faced with when modelling unsteady flows of Bingham fluids, namely the usual problems raised by the mathematical properties of the differential operator of advection, the non-differentiability of the constitutive law and the incompressibility condition.

The Galerkin method is known to be particularly efficient in solving elliptic or parabolic equations but to underperform when applied with no regularizing strategy to convection-dominated flows. To address this problem, we turned to a characteristic/Galerkin formulation. When applied to Newtonian flows, this formulation is known to lead to stable and convergent numerical schemes under a condition that is weaker than the CFL condition, see a.o. [13]. Moreover, it results in solving linear symmetrical algebraic problems only.

Shear stresses are not determined by the Bingham constitutive model when the shear strain rate magnitude vanishes. Several authors have proposed approximating this model by replacing the non-differential part of the internal dissipation potential by a functional that is differentiable at least once for any shear strain rate. In the case of the Tanner's [2] bi-viscous model, the law is modified only for small magnitudes of the shear strain rate, as the solid regime is replaced by a very viscous regime (with a "plastic viscosity" as numerical parameter). Other authors have proposed modifications that hold for any shear strain rate and lead to highly regular dissipation potential. Of these last models, Panastasiou's [17] exponential model is to our knowledge the most frequently quoted in the literature. Fortin and Glowinsky, see [10, Chapter III] and [12, Chapter VI], in contrast have proposed an application of their decomposition/coordination method to deal with the unregularized constitutive law (1) and (2). This strategy has been adopted by Fortin et al. [9] in case of steady flows and by Huilgol and Panizza [14] and recently by Roquet and Saramito [18] in case of pipe flows. The difficulty due to the constitutive law is isolated from others by introducing a new primal variable γ that represents the shear strain rate tensor (decomposition step) and a Lagrange multiplier λ that enforces the constraint $\gamma = D(u)$, making sense to this new primal variable (coordination step by a penalisation–dualisation technique). No continuity assumption is required for these new variables which belong to $\mathscr{W} = [w \text{ such that } w_{ij} \in \mathscr{L}^2(\Omega)]$. Subsequently choosing the corresponding discrete fields as piecewise constant functions will turn the discrete counterpart of the constitutive law (3) into a simple analytic relation on each finite element. Furthermore, the interpretation of the Bingham variational inequality with Lagrange multipliers of Duvaut and Lions [8] has been used recently by Dean and Glowinsky [7] to design another method to cope with the unregularized law (1) and (2).

The problem of analysing the regularity that can be expected for the solution of the Bingham problem is still an open problem (see the recent contribution of Fuchs and Seregin [11]), but it seems unreasonable to hope for more than something weaker than $\mathscr{H}^2(\Omega)^d$, whatever the regularity of the right hand member may be. One may note however that in specific cases such as Poiseuille flows in cylindrical pipes [12] or Couette flows, the velocity is known to belong to $\mathscr{H}^s(\Omega),\ s < 5/2$. Due to this lack of regularity we have been led naturally to use piecewise linear approximations of the velocity field. Moreover, this choice, together with the choice of piecewise constant elements for the approximation of γ, allows the constraint $\gamma = D(u)$ to be satisfied exactly. The two finite element spaces for the velocity field and the pressure field should fulfill the discrete Babuska–Brezzi or inf–sup condition, which is known to be impossible if they are based on polynomials of an order less than or equal to one. We have chosen piecewise linear polynomials on triangles for approximating the velocity field and the pressure field (P1/P1 mixed finite elements) and to stabilize the discrete set of equations by adding the Brezzi–Pitkäranta perturbation (see [4]). The numerical analysis of the Brezzi–Pitkäranta stabilization in the case of Bingham fluids can be found in a forthcoming paper [15].

In the next section, we outline the main steps that lead to the fully discrete problem. Then in the last section, we propose validating our numerical strategy using two benchmarks that have been widely used to assess the potentialities of numerical schemes for Newtonian flows, namely the lid-driven cavity and the thermally driven square cavity.

2. Numerical strategy

This section is devoted to the description of the proposed numerical strategy. We do not go into details of any theoretical justification here.

The time interval $]0, T]$ is divided into sub-intervals $]t^n, t^{n+1}]$ assumed for the sake of readability to be of equal length δt. We assume that all solutions up to time $t = t^n$ are known, and we are searching for the solution of (4), (3) and (5) at time t^{n+1}. For all $0 \leqslant n \leqslant N = T/\delta t$, u^n will stand for the approximation of the velocity at time t^n, i.e., $u^n(x) \approx u(x, t^n)\ \forall x \in \Omega$.

The characteristic/Galerkin method relies on decoupling between the advection and diffusion operators of the momentum balance equation (4). The material (total) derivative of the velocity with respect to time

$$\rho\frac{\mathrm{d}u}{\mathrm{d}t}(x,t^{n+1})=\rho\left(\frac{\partial u}{\partial t}(x,t^{n+1})+(u(x,t^{n+1}).\nabla)u(x,t^{n+1})\right)=\nabla\cdot\tau(x,t^{n+1})-\nabla p(x,t^{n+1})+\rho g(x)$$

is approximated using the first-order Euler (backward) scheme by

$$\frac{\mathrm{d}u}{\mathrm{d}t}(x,t^{n+1})\approx\frac{u^{n+1}(x)-u^{n}(\xi_x^{n+1}(t^n))}{\delta t},$$

where $\forall x\in\Omega,\ \xi_x^{n+1}:[t^n,t^{n+1}]\to\mathbb{R}^2$ denotes the characteristic curve that is solution of the final value problem

$$\begin{cases}\dfrac{\mathrm{d}\xi_x^{n+1}(t)}{\mathrm{d}t}=u^n(\xi_x^{n+1}(t)) & \forall t\in[t^n,t^{n+1}],\\ \xi_x^{n+1}(t^{n+1})=x.\end{cases}$$

In its turn this last curve is approximated by $\xi^*:[t^n,t^{n+1}]\to\mathbb{R}^2$:

$$\xi^*(t)=x-(t^{n+1}-t)u^n(x). \tag{6}$$

Finally, the semi-discrete scheme consists of two steps solved successively.

(1) *Convective step*: for all $x\in\Omega$, find

$$u^*(x)=u^n(\xi^*(t^n)).$$

(2) *Diffusive step*: find $u^{n+1}\in\mathscr{U}=\{v\in\mathscr{V}|\nabla\cdot v=0\}$, such that

$$\rho\frac{u^{n+1}(x)-u^*(x)}{\delta t}=\nabla\cdot\tau^{n+1}(u^{n+1})-\nabla p^{n+1}+\rho g,$$

where $\mathscr{V}=\mathscr{X}^2=[\mathscr{H}_0^1(\Omega)]^2$. The rest of the section is devoted to the diffusive step. By introducing the auxiliary variable $\gamma=D(u)$ and by a suitable choice of vector f, this latter problem can be reformulated as follows.

Problem 1. Find $(u,\gamma)\in\{(v,w)\in\mathscr{U}\times\mathscr{W}|\nabla\cdot v=0,w=D(v)\}$ such that

$$\mathscr{G}(u)+\mathscr{F}(\gamma)=\min_{(v,w)}[\mathscr{G}(v)+\mathscr{F}(w)],$$

where

$$\mathscr{G}(v)=\frac{\rho}{2\delta t}\int_\Omega v\cdot v\,\mathrm{d}\Omega-\int_\Omega f\cdot v\mathrm{d}\Omega\quad\text{and}\quad\mathscr{F}(w)=\int_\Omega\psi(w)\,\mathrm{d}\Omega.$$

The constraints $\nabla\cdot u=0$ and $\gamma=D(u)$ are relaxed by introducing two Lagrange multipliers p and λ leading to the following saddle point problem.

Problem 2. Find $(u,\gamma,p,\lambda)\in\mathscr{V}\times\mathscr{W}\times\mathscr{Q}\times\mathscr{W}$ such that

$$\mathscr{L}_r(u,\gamma,p,\lambda)=\inf_{(v,w)\in\mathscr{V}\times\mathscr{W}}\left(\sup_{(q,v)\in\mathscr{Q}\times\mathscr{W}}\mathscr{L}_r(v,w,q,v)\right),$$

where $\mathscr{L}_r$ stands for the Lagrangian functional defined on $\mathscr{V}\times\mathscr{W}\times\mathscr{Q}\times\mathscr{W}$ by

$$\mathscr{L}_r(v,w,q,v) = \mathscr{G}(v) + \mathscr{F}(w) - \langle v, w - D(v)\rangle_{\mathscr{W}} - \langle \nabla\cdot v, q\rangle_{\mathscr{Q}} + \frac{r_1}{2}\|w - D(v)\|^2_{\mathscr{W}} + \frac{r_2}{2}\|\nabla\cdot v\|^2_{\mathscr{Q}},$$

where $\mathscr{Q} = \mathscr{L}^2_0(\Omega)$ stands for the set of admissible pressures and r_1, r_2 are two penalty parameters.

Next, we introduce the discrete counterparts of sets $\mathscr{V}$, $\mathscr{Q}$ and $\mathscr{W}$. We assume that a finite element regular and quasi-uniform partition $\mathscr{T}_h$ of $\bar{\Omega}$ into polyhedrons (for a precise definition, see [5]) exists with $\mathscr{T}_h = \bigcup_{K\in\mathscr{T}_h}(K)$. The discretization parameter h is defined by $h = \sup_{K\in\mathscr{T}_h}(h_K)$, where h_K denotes the diameter of the smallest circle including the polyhedron K. Each polyhedron $K \in \mathscr{T}_h$ is associated with three Lagrange finite elements [5] $(K, \varphi_K, \Sigma^{\varphi}_K)$, $(K, \pi_K, \Sigma^{\pi}_K)$ and $(K, \psi_K, \Sigma^{\psi}_K)$ that correspond to each component of the velocity field, the pressure field and each component of the shear strain rate field, respectively. We set $\mathscr{V}_h$, $\mathscr{Q}_h$ and $\mathscr{W}_h$ for the discretized sets of admissible velocities, admissible pressures, and admissible shear strain rates respectively, where

$$\mathscr{V}_h = [\mathscr{X}_h]^2 = \left[\left\{v_i \in \mathscr{C}^0(\bar{\Omega}) \text{ such that } v_i|K \in \varphi_K \ \forall K \in \mathscr{T}_h\right\}\right]^2 \subset \mathscr{V},$$

$$\mathscr{Q}_h = \left\{q \in \mathscr{L}^2(\bar{\Omega}) \text{ such that } q_{|K} \in \pi_K \ \forall K \in \mathscr{T}_h\right\} \subset \mathscr{Q},$$

$$\mathscr{W}_h = \left[\left\{w_{i,j} \in \mathscr{L}^2(\bar{\Omega}) \text{ such that } w_{i,j}|K \in \psi_K \ \forall K \in \mathscr{T}_h\right\}\right]^{2\times 2} \subset \mathscr{W}.$$

We can state a discrete analogue of problem 2.

Problem 3. Find $(u_h, \gamma_h, p_h, \lambda_h) \in \mathscr{V}_h \times \mathscr{W}_h \times \mathscr{Q}_h \times \mathscr{W}_h$ such that

$$\begin{aligned}
&\mathscr{L}_h(u_h,\gamma_h,p_h,\lambda_h) \leqslant \mathscr{L}_h(v_h,\gamma_h,p_h,\lambda_h) \quad \forall v_h \in \mathscr{V}_h,\\
&\mathscr{L}_h(u_h,\gamma_h,p_h,\lambda_h) \leqslant \mathscr{L}_h(u_h,w_h,p_h,\lambda_h) \quad \forall w_h \in \mathscr{W}_h,\\
&\mathscr{L}_h(u_h,\gamma_h,p_h,\lambda_h) \geqslant \mathscr{L}_h(u_h,\gamma_h,q_h,\lambda_h) \quad \forall q_h \in \mathscr{Q}_h,\\
&\mathscr{L}_h(u_h,\gamma_h,p_h,\lambda_h) \geqslant \mathscr{L}_h(u_h,\gamma_h,p_h,v_h) \quad \forall v_h \in \mathscr{W}_h,
\end{aligned}$$

where $\mathscr{L}_h$ stands for the augmented Lagrangian functional defined on $\mathscr{V}_h \times \mathscr{W}_h \times \mathscr{Q}_h \times \mathscr{W}_h$ by

$$\begin{aligned}
\mathscr{L}_h(v_h,w_h,q_h,v_h) = {} & \mathscr{G}(v_h) + \mathscr{F}(w_h) - \langle v_h, w_h - D(v_h)\rangle_{\mathscr{W}} - \langle \nabla\cdot v_h, q_h\rangle_{\mathscr{Q}} + \frac{r_1}{2}\|w_h - D(v_h)\|^2_{\mathscr{W}}\\
& + \frac{r_2}{2}\|\nabla\cdot v_h\|^2_{\mathscr{Q}} - \frac{\alpha}{2}\sum_{K\in\mathscr{T}_h} h_K^2\|\nabla q_h\|^2_K.
\end{aligned}$$

The last term in the Lagrangian functional $\mathscr{L}_h$ is the Brezzi–Pitkäranta perturbation, necessary to cope with the instability of the chosen pair of velocity and pressure approximation spaces. Rules for optimal choices of the perturbation parameter α can be found for regular grids in [20]. Once this term is introduced, the problem loses its standard saddle point structure.

Finally as already mentioned, sets φ_K and π_K are assumed to be the sets of linear functions on K whereas set ψ_K is assumed to be the set of functions that remain constant over K. The algorithm we used to solve Problem 3 is an extension of the fully decoupled algorithm ALG2 of [10,12] and thus also an extension of the Uzawa algorithm. It reads:

Algorithm 1. $(u_h^{l-1}, \gamma_h^{l-1}, p_h^{l-1}, \lambda_h^{l-1})$ being known, find $(u_h^l, \gamma_h^l, p_h^l, \lambda_h^l)$ solving the following four steps successively, $\forall (v_h, w_h, q_h, v_h) \in \mathscr{V}_h \times \mathscr{W}_h \times \mathscr{Q}_h \times \mathscr{W}_h$:

- $\langle \mathscr{G}'(u_h^l); v_h - u_h^l \rangle_{\mathscr{V}_h} - \langle p_h^{l-1}; \nabla \cdot (v_h - u_h^l) \rangle_{\mathscr{Q}_h} + \langle \lambda_h^{l-1}; \nabla(v_h - u_h^l) \rangle_{\mathscr{W}_h} + r_1 \langle \nabla u_h^l - \gamma_h^{l-1}; \nabla(v_h - u_h^l) \rangle_{\mathscr{W}_h} + r_2 \langle \nabla \cdot u_h^l; \nabla \cdot (v_h - u_h^l) \rangle_{\mathscr{Q}_h} \geqslant 0.$

- $\mathscr{F}_1(w_h) - \mathscr{F}_1(\gamma_h^l) + \langle \mathscr{F}_0'(\gamma_h^l); w_h - \gamma_h^l \rangle_{\mathscr{W}_h} - \langle \lambda_h^{l-1}; w_h - \gamma_h^l \rangle_{\mathscr{W}_h} + r_1 \langle w_h - \nabla u_h^l; w_h - \gamma_h^l \rangle_{\mathscr{W}_h} \geqslant 0.$

- $\langle p_h^l - p_h^{l-1}; q_h \rangle_{\mathscr{Q}_h} = -\rho_2 \left[\langle \nabla \cdot u_h^l; q_h \rangle_{\mathscr{Q}_h} + \alpha \sum_{K \in \mathscr{T}_h} h_K^2 \langle \nabla p_h^l; \nabla q_h \rangle_{\mathscr{Q}_h} \right].$

- $\langle \lambda_h^l - \lambda_h^{l-1}; v_h \rangle_{\mathscr{W}_h} = -\rho_1 \langle \gamma_h^l - \nabla u_h^l; v_h \rangle_{\mathscr{W}_h},$

where $\mathscr{F}_0$ and $\mathscr{F}_1$ denote the differentiable and non-differentiable parts of the functional $\mathscr{F}$, respectively. The optimality condition associated to γ (second step of the algorithm) takes the form of the following series of minimization problems.

Problem 4. For all $K \in \mathscr{T}_h$, find γ_K^l that minimizes the functional:

$$\theta(w_h) = \int_K \left[\left(\mu + \frac{r_1}{2} \right) \|w_h\|^2 + \tau_Y \|w_h\| - (\lambda_K^{l-1} + r_1 D(u_h^l)) : w_h \right] \mathrm{d}\Omega,$$

Each of those problems can be solved analytically. We define

$$\zeta_K^l = \lambda_K^{l-1} + \frac{r_1}{\int_K \mathrm{d}\Omega} \int_K D(u_h^l)\, \mathrm{d}\Omega$$

and, over each triangle, the shear strain rate is given explicitly by

$$\begin{cases} \text{if } \|\zeta_K^l\| < \tau_Y & \gamma_K^l = 0, \\ \text{if } \|\zeta_K^l\| \geqslant \tau_Y & \gamma_K^l = \dfrac{1}{2\left(\mu + \frac{r_1}{2}\right)} \left(1 - \dfrac{\tau_Y}{\|\zeta_K^l\|} \right) \zeta_K^l. \end{cases}$$

This last aspect represents the main interest of the decomposition-coordination technique.

This method has been implemented in C++ as an application of PELICANS, an object oriented platform developed by our team to provide general frameworks and software components for the implementation of PDEs solvers.

3. Numerical experiments

3.1. Flow in the lid-driven cavity

This section is devoted to our contribution to the lid-driven cavity benchmark. This benchmark has been extensively used for Newtonian fluids to test CFD codes. A fluid fills up the unit square cavity $(0 \leqslant (x, y) \leqslant 1)$ whose upper boundary $(y = 1)$ moves with uniform horizontal velocity while the three other

sides remain motionless. The fluid is assumed to stick to the cavity walls. Even if, strictly speaking, the restriction of the velocity to the boundary is discontinuous, this difficulty is eliminated when dealing with the piecewise linear discrete velocity and neither regularization nor specific numerical treatment is necessary. We then impose strict Dirichlet conditions on the degrees of freedom associated to the velocity. Obviously we are concerned here with the extension of this conventional benchmark to Bingham fluid flows.

For this particular flow, the main quantitative results that can be given are the features of the flow vortices (intensity, center location). To this end, we need to compute the stream function ψ on the whole domain as a post-process, by solving the following PDE:

$$\nabla^2\psi(x,y) = \frac{\partial u_y}{\partial x} - \frac{\partial u_x}{\partial y}.$$

This equation admits a weak form posed on $\mathscr{X}$ that is replaced by its Galerkin approximation posed on $\mathscr{X}_h$. Each vortex is then characterized by a local extremum of this piecewise linear discrete stream function, its intensity being equal to the absolute value of this local extremum.

All the following results have been obtained using the numerical strategy presented in section 2, with zero yield stress in case of Newtonian fluid. We use uniform meshings made up of triangles and that keep the symmetry properties of the square. In the next two subsections that are devoted to creeping flows and to unsteady flows, respectively, we start by a comparison with standard results obtained for Newtonian fluids, then we display the results we obtain for various values of the yield stress. In all the calculations, the fluid viscosity has been set to 1 Pa s as the density is either zero (creeping flows) or 1000 $\mathrm{kg/m^3}$.

Validations on Newtonian fluid flows have been made by comparison with highly accurate results obtained with the Chebyshev collocation method or from literature by Botella and Peyret [3].

3.1.1. Creeping flows

We first focus on creeping flows, which will allow us to compare our results with previously published ones. In Table 1, we display the results obtained for a vanishing yield stress using finer and finer meshes. With regard to the principal vortex, these results tally well with the reference results. The symmetrical secondary vortices are not found with the coarsest mesh. A 80×80 mesh is necessary to capture all the flow features accurately (relative error on the intensity of $7 \times 10^{-2}\%$ for the principal vortex and 1% for the secondary vortices). In Table 1, the abbreviation undisc. stands for a result that has not been disclosed. On Fig. 1 we have plotted the spatial distribution of the streamlines and of the rigid zones (i.e. zones where the shear strain rate vanishes) obtained for various values of the yield stress. One observes the growth of the rigid zones already reported by other authors, see among others [1,16,19].

Table 1
Features of vortices in case of a Newtonian fluid

Reference		Principal vortex		Bottom left vortex	
		Intensity	Position	Intensity	Position
Present work	20×20 mesh	0.09978	$(0.5, 0.75)$	Absent	
	40×40 mesh	0.09991	$(0.5, 0.775)$	1.76×10^{-6}	$(0.025, 0.05)$
	80×80 mesh	0.100054	$(0.5, 0.7625)$	2.25×10^{-6}	$(0.0375, 0.0375)$
	160×160 mesh	0.100072	$(0.5, 0.7625)$	2.235×10^{-6}	$(0.0375, 0.0375)$
Botella and Peyret [3]		0.10008	undisc.	2.223×10^{-6}	undisc.
Mitsoulis and Zisis [16]		0.0995	(0.5,0.7625)	undisc.	

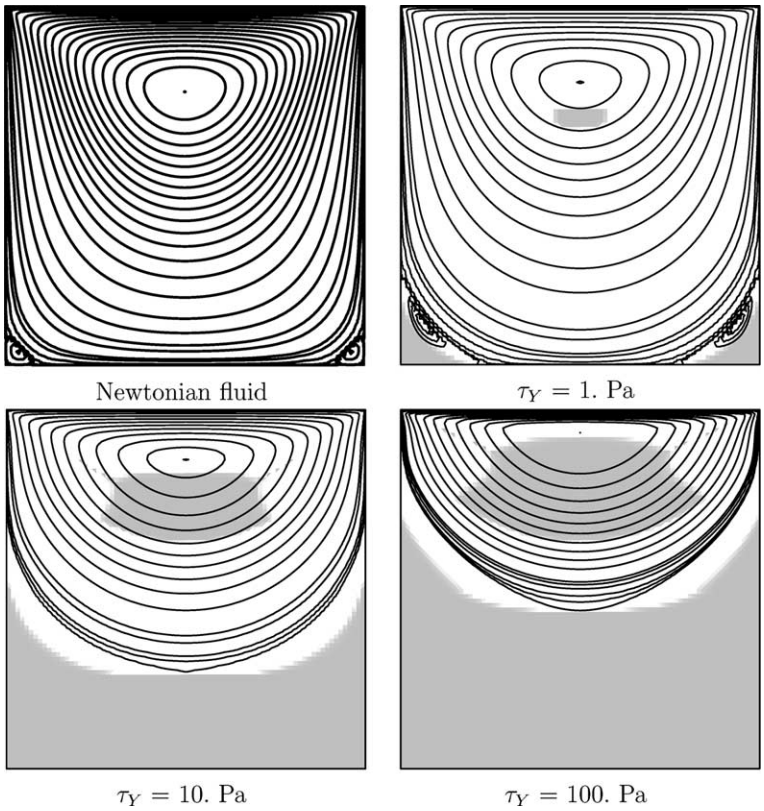

Fig. 1. Streamlines and rigid zones, $Re = 0$.

The secondary vortices that are observed for a Newtonian fluid remain present for low yield stress values. They are then pushed up by the growth of rigid zones while their intensity decreases and finally they disappear. The evolution of the principal vortex features is compared to the results of the computations performed by Mitsoulis and Zisis [16] with a regularized constitutive law on Fig. 2. The step-shaped curve of Fig. 2 corresponding to the present work is due to the piecewise linear approximation of the stream function.

The horizontal velocity evolution along the vertical centerline shown in Fig. 3 again highlights the progressive growth of the rigid zones. As the value of the yield stress rises, the principal vortex center goes up toward the upper cavity side, the zone dragged by the upper boundary becomes thinner and thinner, presenting increasingly steep gradients, while the flow return zone becomes homogeneous and remains broad. For highest values of the yield stress, the problem approaches the extreme situation of an incompressible solid square blocked along three of its edges and driven along the last one, and no flow can be observed except for the upper layers of elements. In this very specific case, adaptative remeshing techniques should have certainly been adopted.

3.1.2. Flow for $Re = 10^3$

We are interested now in the steady solution for a Reynolds number of 10^3, which we obtain by transient computation pursued up to the time step when the following criterion is fulfilled:

$$\frac{|u_h^{n+1} - u_h^n|_\infty}{\delta t |u_h^{n+1}|_\infty} < 10^{-6}.$$

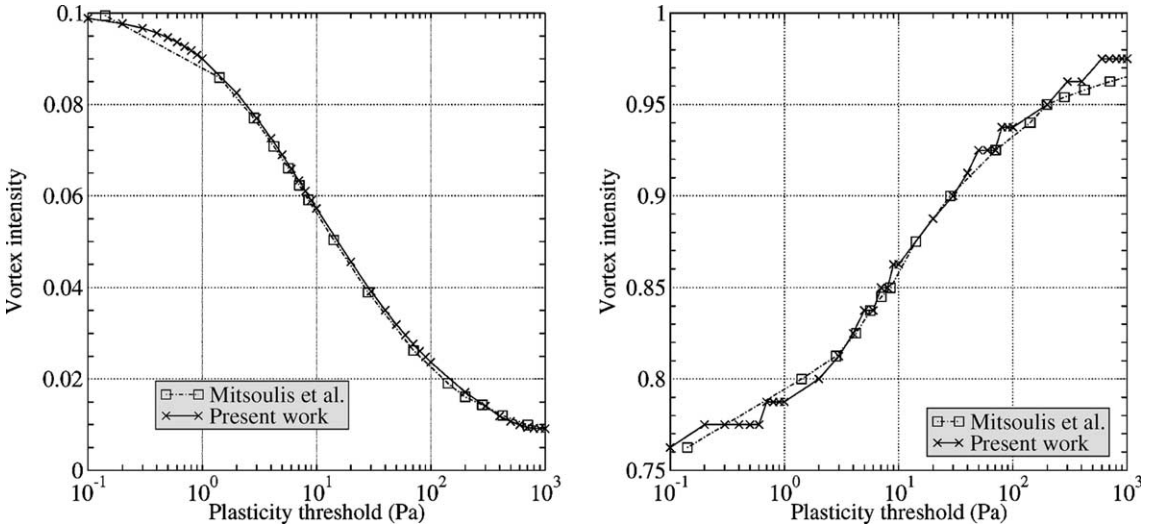

Fig. 2. Principal vortex intensity and ordinate, $Re = 0$.

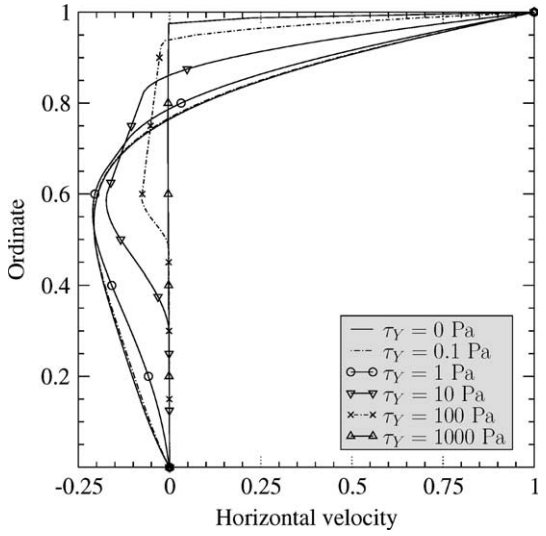

Fig. 3. Section of the horizontal velocity, $Re = 0$.

We start this section anew by validating our numerical method against results in literature for Newtonian fluid flows. In Table 2, we present the features of the three vortices, i.e., the principal and the two secondary vortices located at the right and left bottom corners of the cavity, respectively. Once again results concur with the results in literature. Then in Fig. 4 we plot the maps of the streamlines and the rigid zones for various yield stress values. Compared to Stokes flow, the disappearance of the secondary vortices and the appearance of rigid zones when raising the yield stress is deferred. At high yield stress values, the inertial effects are softened and once again a solution similar to that of Stokes problem is found.

The evolution of the principal vortex features as a function of the yield stress is drawn in Fig. 5. Fig. 6 shows the evolution of the horizontal and vertical velocities along the vertical and horizon-

Table 2
Features of vortices in case of a Newtonian fluid

Reference	Principal	Bottom right	Bottom left
Present work 80×80 mesh	0.1162 $(0.525, 0.5625)$	1.70×10^{-3} $(0.8625, 0.1125)$	2.1×10^{-4} $(0.0875, 0.075)$
Botella and Peyret [3]	0.1189 $(0.531, 0.5652)$	1.73×10^{-3} $(0.864, 0.118)$	2.3×10^{-4} (0.0833,0.0781)
Other references of Botella and Peyret [3]	$[0.113, 0.119]$	$[1.6 \times 10^{-3},\ 1.9 \times 10^{-3}]$	$[2.1 \times 10^{-4}, 3.2 \times 10^{-4}]$

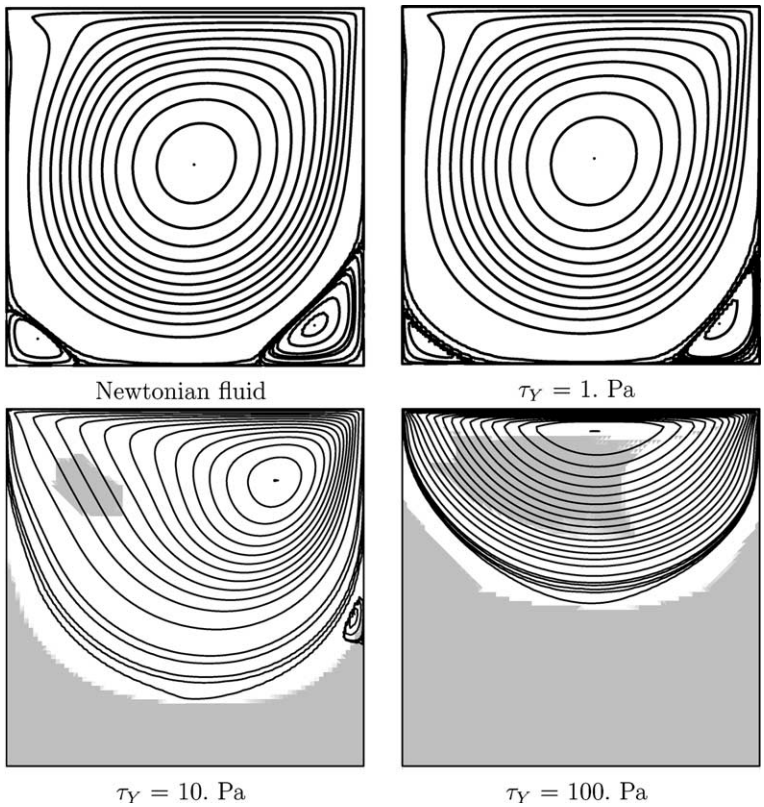

Fig. 4. Streamlines and rigid zones, $Re = 10^3$.

tal centerline, respectively, while the position and value of the extrema of these curves are given in Table 3.

3.2. Thermally driven cavity

This numerical experiment consists of an extension of the benchmark proposed by De Vahl Davis [6] to fluids with yield stress. Briefly, the fluid is assumed to fill the unit square cavity completely and to stick to its

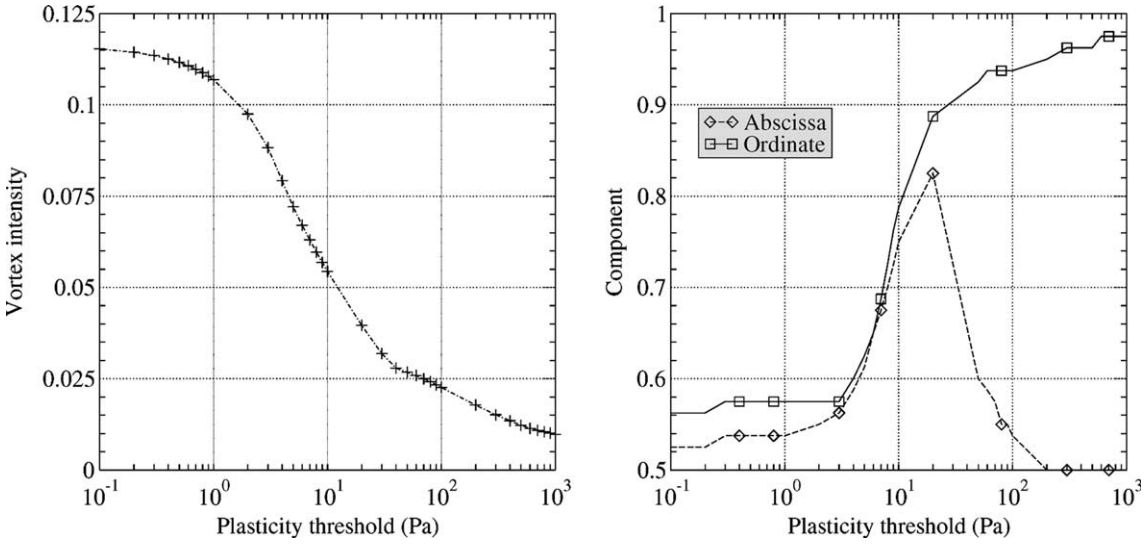

Fig. 5. Principal vortex intensity and position, $Re = 10^3$.

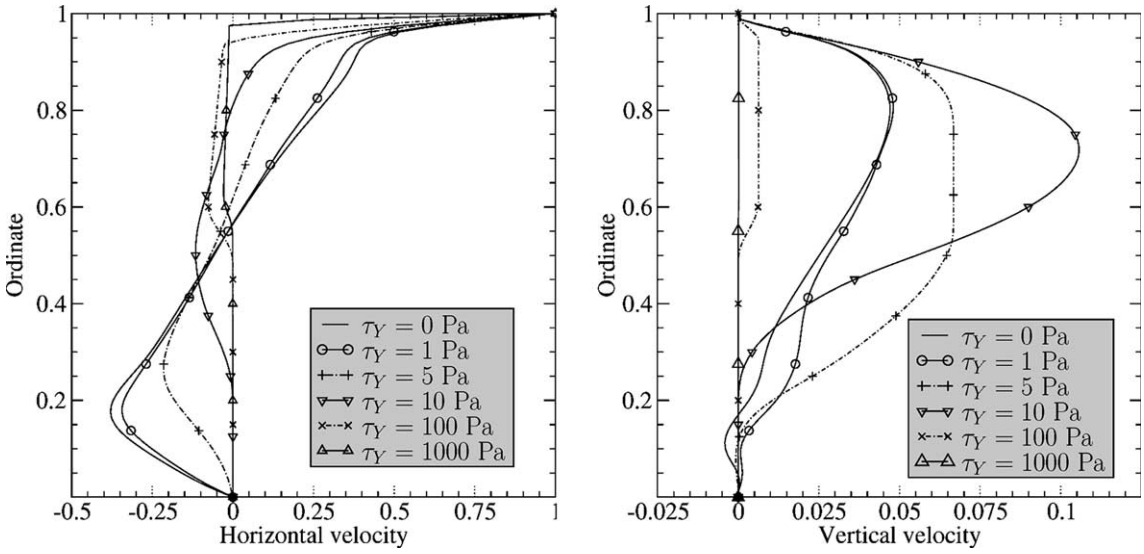

Fig. 6. Sections of velocity along the vertical mid-plane, $Re = 10^3$.

four walls. The vertical walls are differentially heated whereas the horizontal ones are assumed to be adiabatic. As already mentioned in section 1, if flows are no longer assumed to be isothermal, coupling with the temperature remains weak as the rheologic properties of the fluid are assumed not to depend on temperature changes. We apply the Boussinesq hypothesis, i.e., all variations of density are neglected except for the gravitational terms where the density is assumed to have linear dependence on temperature changes. The fluid motion is governed by the Boussinesq system of equations, i.e., by the momentum balance equation

Table 3
Velocity extrema along centerlines $x = 0.5$ and $y = 0.5$

References	Extrema of velocities along centerlines					
	Along $x = 0.5$		Along $y = 0.5$			
	$y_{\min}$	$\min_y V_x$	$x_{\min}$	$\min_x V_y$	$x_{\max}$	$\max_x V_y$
Botella and Peyret [3]	0.1717	−0.3886	0.9092	−0.5271	0.1578	−0.3769
Other references of Botella and Peyret [3]	[0.16, 0.18]	[−0.39, −0.37]	[0.90, 0.91]	[0.49, 0.53]	[0.15, 0.16]	[−0.38, −0.34]
$\tau_Y = 0$ Pa	0.175	−0.3813	0.9125	−0.5181	0.1625	0.3723
$\tau_Y = 0.1$ Pa	0.175	−0.3796	0.9125	−0.5144	0.1625	0.364
$\tau_Y = 1$ Pa	0.175	−0.3438	0.9	−0.482	0.1625	0.3286
$\tau_Y = 5$ Pa	0.2625	−0.2149	0.8875	−0.3373	0.225	0.1786
$\tau_Y = 10$ Pa	0.5	−0.1156	0.825	−0.1258	0.3375	0.0572
$\tau_Y = 100$ Pa	0.6	−0.0762	0.6125	−0.0002	0.4625	0.00017
$\tau_Y = 1000$ Pa	0.6375	−0.0288	0.925	−0.00015	0.075	0.00016

$$\rho\left(\frac{\partial u}{\partial t} + (u.\nabla)u\right) - \nabla \cdot \sigma = \rho(1 - \beta(T - T_{\text{ref}}))g,$$

where β, T and T_{ref} denote the thermal expansion coefficient, temperature field and a reference temperature, respectively, by the energy balance equation

$$\frac{\partial T}{\partial t} + (u \cdot \nabla)T = k\Delta T, \tag{7}$$

where k denotes the thermal diffusivity, by continuity Eq. (5), by the constitutive relations (1) and (2) and by Dirichlet homogeneous boundary conditions on the Lipschitz domain boundary $\partial\Omega$. The splitting scheme of section 2 is modified to include the energy balance equation (7):

(1) *Convective step*: for all $x \in \Omega$, find

$$u^*(x) = u^n(\xi^*(t^n)), \quad T^*(x) = T^n(\xi^*(t^n)),$$

where $\xi^*(t^n)$ is defined by (6).

(2) *Diffusive step*: find $T^{n+1} \in \mathscr{X}$ and $u^{n+1} \in \mathscr{U} = \{v \in \mathscr{V} | \nabla \cdot v = 0\}$, such that

$$\frac{T^{n+1}(x) - T^*(x)}{\delta t} = k\Delta T^{n+1}(x),$$

$$\frac{u^{n+1}(x) - u^*(x)}{\delta t} = \nabla \cdot \tau^{n+1}(u^{n+1}) - \nabla p^{n+1} + \rho g.$$

Modification of the convection step due to processing the energy balance is straightforward as the characteristic curves have already been computed for the velocity advection step. The temperature diffusion step leads to the resolution of a second order elliptic PDE.

We detail here computations performed at a rather low Rayleigh number value, $Ra = 10^4$, for which complete fluid blocking is obtained for reasonable yield stress values. Then we give some of the results obtained at higher Rayleigh numbers.

The computations have been performed with the following physical parameters values: $\rho = 1$ kg/m^3, viscosity of 1 Pa s, $k = 1$ m^2/s, $g = 10$ m^2/s, and $\beta/Ra = 7.1 \times 10^{-2}$ K^{-1}.

Table 4
Comparison with the benchmark solution of [6], Newtonian fluid

	Meshing 20×20	Meshing 40×40	Meshing 60×60	Benchmark [6]
Nu^0	2.205	2.235	2.240	2.238
$Nu^{\max}(z)$	3.384 (0.15)	3.482 (0.15)	3.497 (0.15)	3.528 (0.143)
$Nu^{\min}(z)$	0.640 (1.)	0.611 (1.)	0.601 (1.)	0.586 (1.)
$\lvert\psi^{\max}\rvert$	4.938	4.999	5.032	5.071
$V_x^{\max}(z)$	15.779 (0.85)	16.028 (0.825)	16.091 (0.833)	16.178 (0.823)
$V_z^{\max}(x)$	19.111 (0.1)	19.38 (0.875)	19.423 (0.117)	19.617 (0.119)

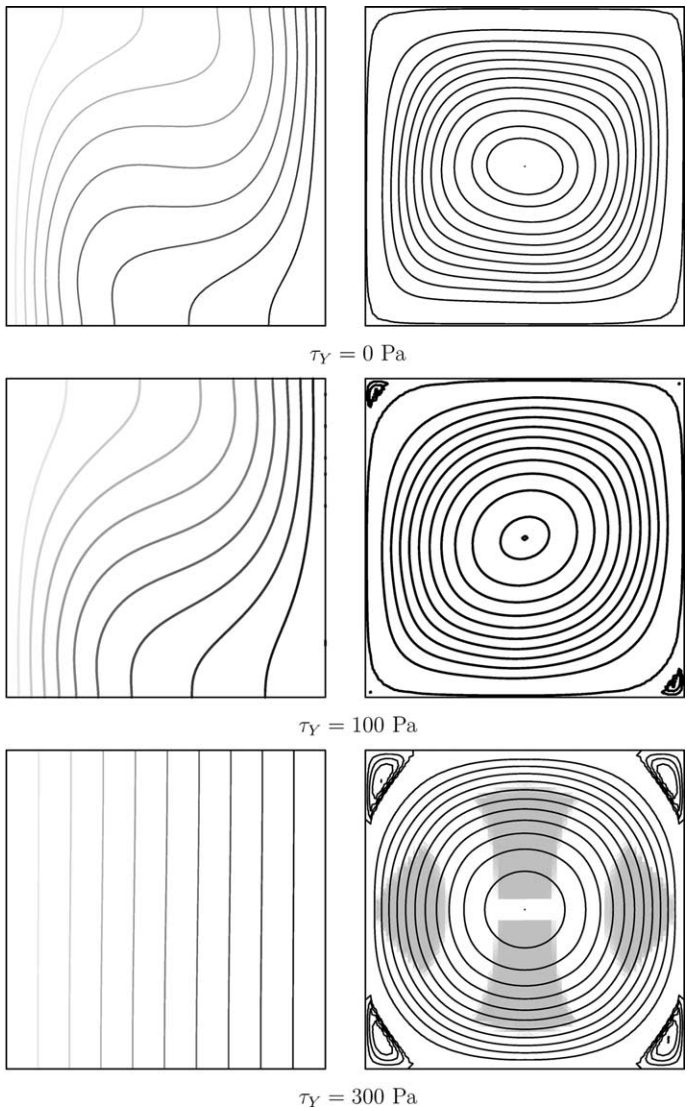

Fig. 7. Temperature field, left column and streamlines and rigid zones, right column, $Ra = 10^4$.

We start once again by validating our numerical strategy in the case of Newtonian fluid flows, by comparing our results with the benchmark results of [6]). In Table 4, we have collected the characteristic flow quantity values proposed by De Vahl Davis: Nu^0, $Nu^{\max}$ and $Nu^{\min}$ are the average, maximal and minimal Nusselt numbers at the left cavity wall, $|\psi^{\max}|$ is the vortex intensity, $V_x^{\max}$ (m/s) is the maximum horizontal component of the velocity at the vertical mid-plane and $V_z^{\max}$ (m/s) is the maximum vertical component of the velocity at the horizontal mid-plane.

We turn next to flows obtained for non-zero values of the plasticity threshold. In Fig. 7 we display spatial distributions of the temperature field, streamlines and rigid zones obtained for various yield stress

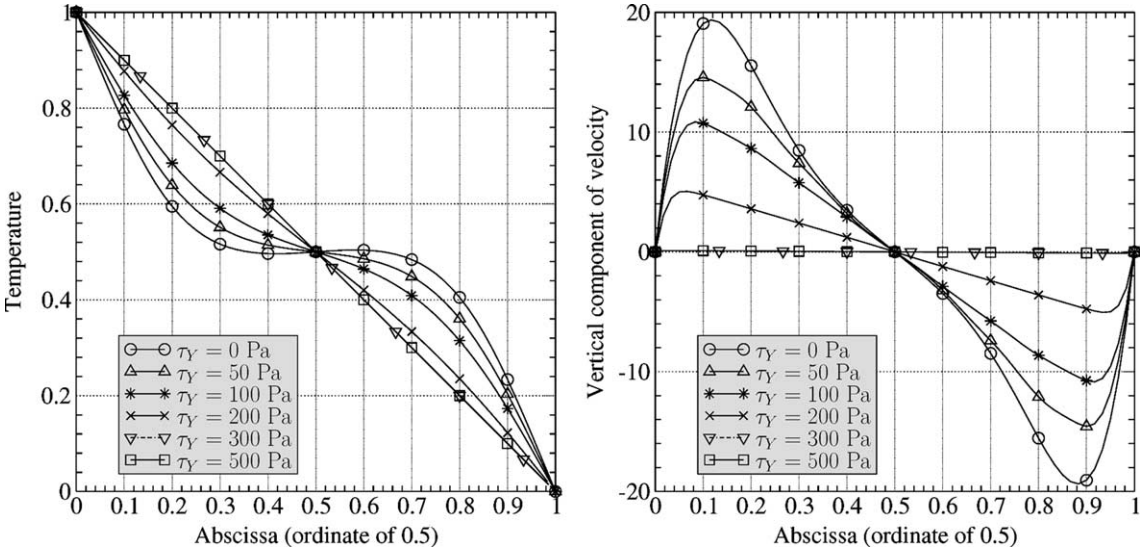

Fig. 8. Temperature and velocity sections for various plasticity thresholds (Pa).

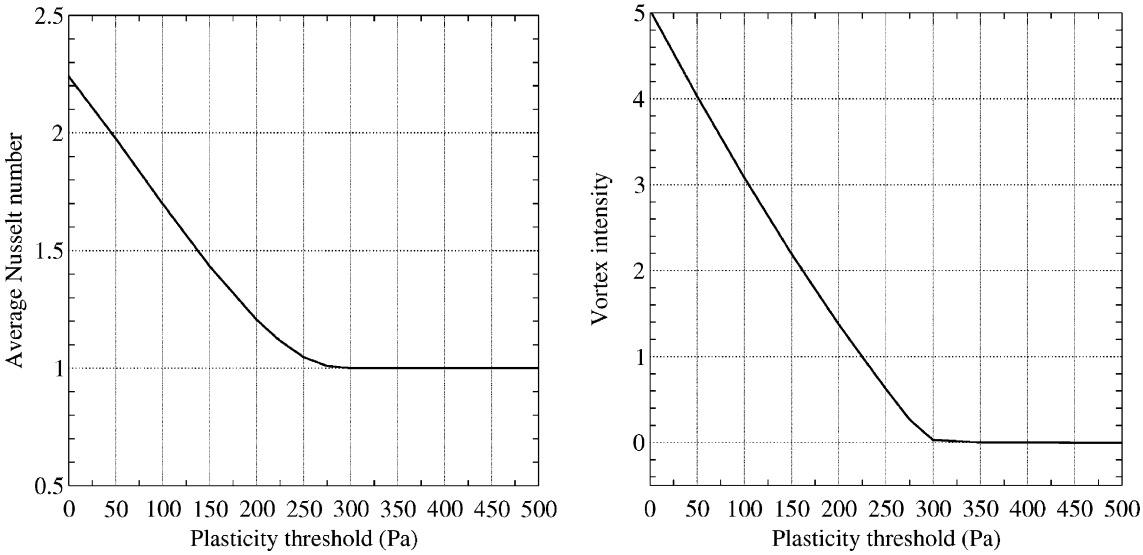

Fig. 9. Nusselt number at hot wall and vortex intensity.

Table 5
Flow characteristics for a yield stress of 300 Pa and various Rayleigh numbers

	$Ra = 10^4$	$Ra = 10^5$	$Ra = 10^6$	$Ra = 10^7$	$Ra = 10^8$
Nu^0	1.0056	4.0127	8.5646	15.76	25.406
$Nu^{\max}(z)$	1.022 (0.08)	6.937 (0.1)	16.71 (0.04)	34.37 (0.02)	54.054 (0.02)
$Nu^{\min}(z)$	0.989 (0.94)	0.6234 (1.)	0.925 (1.)	1.478 (1.)	2.7136 (1.)
$\lvert\psi^{\max}\rvert$	$3.76\ 10^{-2}$	8.8365	16.64	30.625	64.455
$V_x^{\max}(z)$	0.139 (0.98)	26.375 (0.85)	58.475 (0.85)	152.71 (0.89)	875.61 (0.97)
$V_z^{\max}(x)$	0.146 (0.01)	52.35 (0.06)	212.873 (0.04)	704.65 (0.02)	2303.09 (0.01)

values. When the yield stress increases, secondary vortices appear at two corners of the cavity, then some rigid zones are observed while tertiary vortices appear at the last two corners. The temperature field turns out to be independent on the ordinate. For a yield stress of 300 Pa, the principal vortex intensity is one hundred times lower than for the Newtonian flow. Then for a yield stress value close to 500 Pa, the fluid is completely blocked and we obtain the analytical linear solution for the temperature field.

This behaviour is more accurately quantified by the temperature and vertical velocity component curves along the horizontal mid-plane shown in Fig. 8. The evolution of the average Nusselt number at the hot wall and of the vortex intensity as a function of the yield stress are presented in Fig. 9.

In Table 5 we finally present the results we obtained for a yield stress value of 300 Pa and for various Rayleigh number values.

4. Conclusion

In this paper, we have presented a numerical method for dealing with Bingham fluid flows which appears to be robust, thus in particular able to cope with convection-dominated problems, and cost-effective, by the use of low order finite elements. Moreover, this latter choice is well suited to the problem in hand because of the poor regularity which can be expected for the solution. In addition, this numerical scheme takes benefit of the use the Fortin–Glowinski decomposition-coordination method to offer wide flexibility in the choice of the rheological constitutive relations; for example, changing from the Bingham law to a more sophisticated one, as the Herschel–Bulkley law, would result in rather straightforward development. The numerical analysis of this scheme, restricted to the Stokes problem, is the topic of a forthcoming paper [15].

Acknowledgements

The authors thank all members of their team for their constant help and professors E. Mitsoulis and Th. Zisis for the results of Tables 1 and 2.

References

[1] M. Bercovier, M. Engelman, A finite-element method for incompressible non-Newtonian flows, J. Comput. Phys. 36 (1980) 313–326.
[2] C.R. Beverly, R.I. Tanner, Numerical analysis of extrudate swell in viscoelastic materials with yield stress, J. Rheol. 33 (1989) 989–1009.
[3] O. Botella, R. Peyret, Benchmark spectral results on the lid-driven cavity flow, Comp. Fluids 27 (4) (1998) 421–433.
[4] F. Brezzi, J. Pitkäranta, On the stabilization of finite element approximations of the Stokes equations, in: W. Hackbusch (Ed.), Efficient Solution of Elliptic Systems, Vieweg, Braunschweig, 1984, pp. 11–19.

[5] P.G. Ciarlet, Basic error estimates for elliptic problems, in: P.G. Ciarlet, J.L. Lions (Eds.), Handbook of Numerical Analysis Volume II: Finite Elements Methods, North-Holland, Amsterdam, 1991.
[6] G. De Vahl Davis, Natural convection of air in a square cavity: a bench mark numerical solution, Int. J. Numer. Meth. Fluids 3 (1983) 249–264.
[7] E.J. Dean, R. Glowinski, Operator-splitting methods for the simulation of Bingham visco-plastic flow, Chin. Ann. Math. B 23 (2002) 187–204.
[8] G. Duvaut, J.L. Lions, Inequalities in Mechanics and Physics, Springer, Berlin, 1976.
[9] A. Fortin, D. Côté, P.A. Tanguy, On the imposition of friction boundary conditions for the numerical simulation of Bingham fluid flows, Comput. Meth. Appl. Mech. Eng. 88 (1991) 97–109.
[10] M. Fortin, R. Glowinski, Méthodes de Lagrangien Augmenté. Application à la résolution numérique de problèmes aux limites, Dunod-Bordas, Paris, 1982.
[11] M. Fuchs, G. Seregin, in: Variational Methods for Problems from Plasticity Theory and for Generalized Newtonian Fluids, Lecture Notes in Mathematics, vol. 1749, Springer, New York, 2000.
[12] R. Glowinski, Numerical Methods for Nonlinear Variational Problems, Springer, New York, 1984.
[13] R. Glowinski, O. Pironneau, Finite element methods for Navier–Stokes equations, Annu. Rev. Fluid Mech. 24 (1992) 167–204.
[14] R.R. Huigol, M.P. Panizza, On the determination of the plug flow region in Bingham fluids through the application of variational inequalities, J. Non-Newtonian Fluid Mech. 58 (1995) 207–217.
[15] J.C. Latché, D. Vola, Analysis of the Brezzi–Pitkaranta stabilized Galerkin scheme for creeping flows of Bingham fluids, submitted for publication in the SIAM Journal of Numerical Analysis.
[16] E. Mitsoulis, T.h. Zisis, Flow of Bingham plastics in a lid-driven square cavity, J. Non-Newtonian Fluid Mech. 101 (2001) 173–180.
[17] T.C. Papanastasiou, Flow of materials with yield, J. Rheol. 31 (1987) 385–404.
[18] N. Roquet, P. Saramito, An adaptive finite element method for viscoplastic fluid flows in pipes, Comput. Meth. Appl. Mech. Eng. 190 (2000) 5391–5412.
[19] F.J. Sanchez, Application of a first-order operator splitting method to Bingham fluid flow simulation, Comput. Math. Appl. 36 (3) (1998) 71–86.
[20] D. Silvester, Optimal low order finite element methods for incompressible flow, Comput. Meth. Appl. Mech. Eng. 111 (1994) 357–368.